

D. EVERSOLE^{1,2}
B. LUK'YANCHUK³
A. BEN-YAKAR^{1,2,4,✉}

Plasmonic laser nanoablation of silicon by the scattering of femtosecond pulses near gold nanospheres

¹ Department of Biomedical Engineering, University of Texas at Austin, Austin, TX 78722, USA

² Center for Nanomaterials, University of Texas at Austin, Austin, TX 78722, USA

³ Data Storage Institute, Agency for Science, Technology and Research, 117608 Singapore

⁴ Department of Mechanical Engineering, University of Texas at Austin, Austin, TX 78722, USA

Received: 29 May 2007 / Accepted: 4 June 2007
Published online: 13 July 2007 • © Springer-Verlag 2007

ABSTRACT We present the fabrication of nanostructures ablated on silicon(100) by the plasmonic scattering of 780 nm, 220 fs laser pulses in the near-field of gold nanospheres. We take advantage of the enhanced plasmonic scattering of ultrashort laser light in the particle near-field to ablate well-defined nanocraters. Gold nanospheres of 150 nm diameter are deposited onto a silicon surface and irradiated with a single laser pulse. We studied the effect of laser polarization on the morphology of ablated nanostructures and estimated the minimum fluence for plasmonic nanoablation. When the polarization of the incident radiation is directed at a 45° angle into the substrate surface, a near-field enhancement of 23.1 ± 7.6 is measured, reducing the required silicon ablation fluence from 191 ± 14 mJ/cm² to 8.2 ± 2.9 mJ/cm². Enhancements are also measured for laser polarizations parallel to the substrate surface when the substrate is angled 0° and 45° to the incident irradiation, giving enhancements of 6.9 ± 0.6 and 4.1 ± 1.3 , respectively. Generated nanocrater morphologies show a direct imprint of the particle dipolar scattering region, as predicted in our theoretical calculations. The measured near-field enhancement values agree well with the maximum field enhancements obtained in our calculations. The agreement between theory and measurements supports that the nanocraters are indeed formed by the enhanced plasmonic scattering in the near-field of the nanoparticles.

PACS 42.62.-b; 52.38.Mf; 81.65.Cf; 81.16.-c; 78.67.Bf

1 Introduction

In recent years, there has been an extensive strive to develop novel laser ablation techniques for the nanomanufacturing of solid materials [1–10, 12–15] as well as for the nanosurgery of biological structures with a submicron resolution [16–19]. Optical near-field technology has been presented as an attractive fabrication method because it spatially confines laser light to nanodomains below the diffraction limit to generate nanometer-scale features. Several near-field optical methods have been developed for nanolithography including, laser assisted scanning-tip patterning [1–4], near-field scanning optical microscope (SNOM) patterning [5–7], plas-

monic lithography [8], contacting particle-lens array (CPLA) utilizing silica beads [9–11], and gold particles [12–15].

Submicron laser surgery techniques currently require the use of tightly focused ultrashort laser pulses to manipulate subcellular structures [16–19]. Limitations arise in the need for the target to be located with submicron resolution and systems are limited by diffraction. To achieve laser confinement below the diffraction limit in biological materials, we propose the use of gold nanoparticles. Noble metal nanoparticles exhibit strong field enhancements in the visible and near-infrared (NIR) wavelengths due to their interband transition properties [20]. These properties make gold nanoparticles good candidates for the manipulation of biological materials for a number of reasons: (1) irradiation by NIR laser light deeply penetrates biological media and (2) gold is a biocompatible material.

In this report, as a first step to demonstrate the concept of Plasmonic Laser Nanoablation/Nanosurgery (PLN), we investigate the nanostructuring of a solid target by the enhanced plasmonic scattering of ultrafast, NIR laser light in the near-field of single, isolated gold nanospheres. Additionally, we believe this study will provide greater understanding in femtosecond laser pulse interactions with gold nanoparticles for solid material modification. The use of femtosecond laser pulses has many distinct advantages [21]: (1) there is a sharp fluence threshold for material modification, which is much lower than picosecond and longer pulse lengths, (2) the rapid energy deposition allows for efficient and precise ablation with reduced thermal and mechanical defects induced to surrounding regions, and (3) production of well-defined structures in any solid material independent of the excitation wavelength. The use of nanometer-sized gold nanospheres provides many other additional benefits. Particles act as “nanolenses”, restricting laser light to the particle’s near-fields, only photodisrupting material located nanometers away, providing nanoscale resolution, and generating surface structures down to a few tens of nanometers in diameter without the need for a tightly focused laser beam. Moreover, the enhanced electro-magnetic field around the particle reduces the amount of required laser fluence for material ablation.

To further understand the plasmonic ablation process, we performed surface ablations on silicon(100) using 150 nm spherical gold nanoparticles and studied generated crater morphology and the minimum fluence required for nanoabla-

✉ Fax: +1-512-471-1045, E-mail: ben-yakar@mail.utexas.edu

tion. The crater structure was directly dependent on particle sizes and laser polarization and fluence. We analyzed nanostructures fabricated by gold nanoparticles irradiated with linearly polarized laser light that was directed in three orientations. Scanning electron microscopy (SEM) and atomic force microscopy (AFM) were used to image ablated nanocraters. Measured near-field enhancements were compared with theoretical values estimated using the solution of the boundary-value problem for a spherical particle on a flat semi-infinite substrate.

2 Experimental approach

2.1 Experimental setup

Figure 1 illustrates the experimental setup. A femtosecond Ti:sapphire laser system (Spitfire, Spectra Physics, Mountain View, CA) delivered laser pulses of 220 fs temporal width and 780 nm wavelength at a 1 kHz repetition rate. An attenuator consisting of a half-wave plate and a polarizing cube beam-splitter was used to control the delivered laser power. Pulse energies were measured before the focusing system using an energy meter (Ophir PL10). The measured pulse energy transmission through the focusing system was estimated to be 64% by finding the ratio of energy before and after the objective. The sample was mounted onto an x - y translational stage. The setup provided simultaneous optical imaging and ablation of the sample through the same objective lens.

We used a long working distance objective lens (0.28 NA, $10\times$; Mitutoya) to focus a linearly polarized laser pulse to a $1/e^2$ radius of $3.2 \pm 0.2 \mu\text{m}$ at the beam waist. In plasmonic ablation experiments, the sample was placed $80 \mu\text{m}$ from the beam waist to obtain a larger spot size. The spot size at this location was estimated based on the linear dependence of the ablation crater diameter, D , with respect to the logarithm of laser energy E_{pulse} [22],

$$D^2 = 2w_0^2 \ln \left(\frac{E_{\text{pulse}}}{E_{\text{pulse,th}}} \right). \quad (1)$$

Here, w_0 is the $1/e^2$ Gaussian beam radius and $E_{\text{pulse,th}}$ is the pulse energy when $D = 0$. Figure 2 plots the diameter of the ablation craters on silicon measured using SEM for various incident laser energies and corresponding fluences. By estimating the slope of the linear fit to the data points, w_0 was determined. At the ablation plane ($z = 80 \mu\text{m}$), the beam was el-

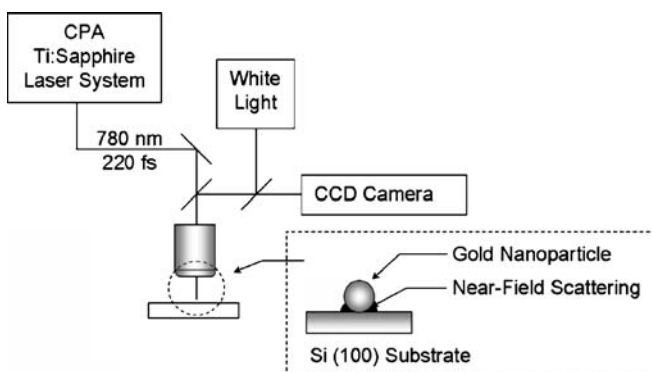


FIGURE 1 Schematic of the femtosecond laser ablation system

liptically shaped such that the measured $1/e^2$ short axis radius was $w_{x0} = 11.1 \pm 0.3 \mu\text{m}$ and the long axis was $w_{y0} = 11.8 \pm 0.2 \mu\text{m}$. The beam ellipticity is attributed to the astigmatic focusing properties of the beam, where the x and y directions of the beam have different focal planes. To determine the quality of the beam in each axis, the relative “ M -squared” value was calculated using the following relationship:

$$w(z) = w_0 \sqrt{1 + \left(\frac{z}{z_R} M^2 \right)^2}, \quad (2)$$

where z_R is the Rayleigh range, z is the distance of propagation, and M^2 is the beam quality. From (2), we find $M_x^2 \approx 1.73$ and $M_y^2 \approx 1.84$, where M_x^2 and M_y^2 correspond to the beam quality in the x and y directions, respectively. Through the direct imaging of optically induced surface changes, this technique provides a precise method for finding laser spot sizes with minimal uncertainties. Measurement uncertainties arise in the curve fitting algorithm and in pulse-to-pulse energy variability of 5%. To obtain a homogeneous, well-defined energy distribution on the target, a circular aperture (6.5 mm in diameter) was placed in the beam path just before the objective. The spatial profile of the truncated beam, originally 8 mm in diameter, was not significantly modulated at the sample plane [23]. All experiments are performed in air at atmospheric pressure.

The orientation of the laser polarization at the sample plane was varied through the manipulation of the sample. When the laser light was directed to be orthogonal to the sample, the laser polarization was parallel to the substrate surface. For the laser to be directed at a 45° angle with respect to the silicon surface, the substrate was mounted onto a standard 45° angle SEM block. By rotating the angled sample 90° , the electric field was either oriented into (p -polarized laser light) or along (s -polarized laser light) the surface plane. The size of the ellipticity of the irradiation zone was modulated as the sample was angled with respect to the laser. The axis of the

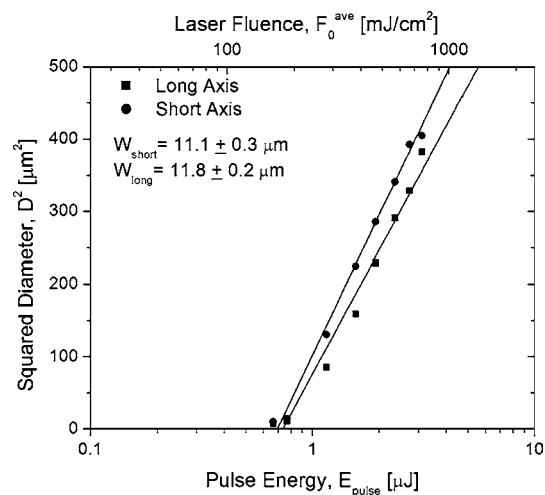


FIGURE 2 The squared diameter of the laser-induced damage on the silicon is plotted as a function of the laser fluence. The slope of the linear fit provides the $1/e^2$ Gaussian beam waist at the plane of ablation. The modification region (i.e., the full extent of damage to the silicon surface due to the irradiation by a single laser pulse) was measured using SEM

beam that was aligned along the angled sample plane was lengthened by a factor $\sqrt{2}$.

2.2 Sample preparation and characterization

A silicon (100) wafer (band gap energy of 1.14 eV) having a 21 Å native oxide layer as measured by ellipsometry was cut into 5 × 5 mm pieces and washed using a four-step process: sulfuric acid, distilled water, acetic acid, and methanol. The wafer was ultrasonicated in each solution for 5 min and stored in methanol until use. A 6 μL aliquot of colloidal gold (2R = 150 nm; British Biocell International) was deposited onto the surface. The sample was annealed in air at 120 °C for five minutes. By using this method, isolated particles could be deposited on the substrate surface.

Before and after irradiation, samples were characterized using SEM and AFM (Dimension 3100; Digital Instruments). The AFM was operated in tapping mode in air, using triangular shaped silicon cantilevers (40.0 N/m spring constant and 300 kHz resonance frequency; Budget Sensors).

2.3 Theoretical considerations in choosing the nanoparticle size

To determine the appropriate particle size to produce the largest field enhancement at 780 nm, we estimated the near-field scattering efficiency, Q_{NF} , of a gold particle embedded in air as a function of its radius. Q_{NF} is a measure of the sphere's ability to convert the incident electric field intensity into a near-field intensity. This quantity, which is proportional to the square of the scattered electric field on the particle surface, E_s , is given by [24]:

$$Q_{\text{NF}} = \frac{R^2}{\pi a^2} \int_0^{2\pi} \int_0^{\pi} E_s E_s^* \sin \theta d\theta d\varphi \Bigg|_{R=a}, \quad (3)$$

where R defines a spherical surface over which the integral is evaluated and a is the particle radius. The near-field quantity consists of all three components of the electric field vector. The angular components, E_θ and E_φ , are perpendicular to the particle surface, while the radial component, E_R , lies normal to the surface. The E_R component, which is proportional to R^{-2} , dominates the scattered field, yielding large fields in the vicinity of the particle. For a given set of sphere parameters, Q_{NF} will be greater than unity, which implies the sphere acts as a field intensifier. This yields local fields larger than that incident on the particle. Figure 3 summarizes the calculations using (3). The plot indicates that the near-field enhancement of a spherical gold particle in air is greatest for particles 150–170 nm in diameter at the 780 nm wavelength. As the particle size increases, phase retardation in electron oscillations leads to multipole resonances which red-shifts the maximal Q_{NF} to longer wavelengths [24, 25]. While having a larger near-field enhancement, 150 nm particles have reduced absorption effects. The dielectric function of gold material reduces with longer wavelengths due to the reduced d -level to sp -band electronic transitions, giving significantly reduced absorption effects. From theoretical Mie calculations we expect 600 times more incident energy to be scattered in the particle near-field than to be absorbed. Since 150 nm gold

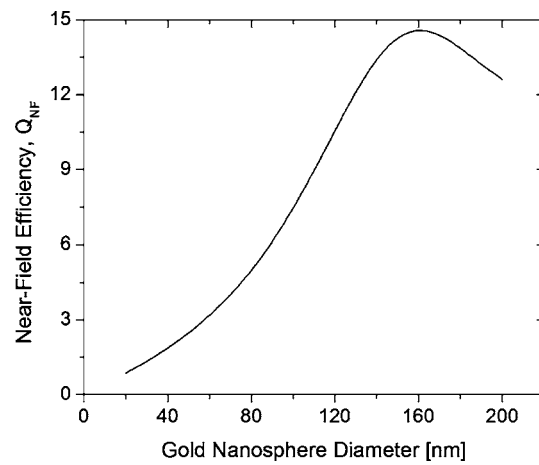


FIGURE 3 Estimated near-field scattering efficiency, Q_{NF} , of gold nanospheres in air as a function of particle diameter. Q_{NF} is a measurement of the particle's ability to convert incident electric field intensity into a near-field intensity. The efficiency term was estimated using (3) according to [26]

particles exhibit large scattering properties in the near-field with minimal absorption effects, they are excellent candidates for plasmonic ablation.

3 Experimental results and analysis

3.1 Femtosecond laser ablation of silicon

Silicon is a material having a low overall femtosecond laser ablation threshold similar to one for metal materials such as gold. A common method for estimating the single-shot ablation threshold of silicon(100) $F_{\text{abl,th}}$ is through the linear relationship between the ablation depth h_a and the average fluence F_0^{ave} [22, 23]:

$$h_a = \alpha_{\text{eff}}^{-1} \ln \left(\frac{F_0^{\text{ave}}}{F_{\text{abl,th}}} \right), \quad (4)$$

where α_{eff}^{-1} is the effective optical penetration depth and $F_{\text{abl,th}}$ is the pulse fluence when $h_a = 0$. Figure 4 presents the ablation depth data measured using AFM for corresponding laser

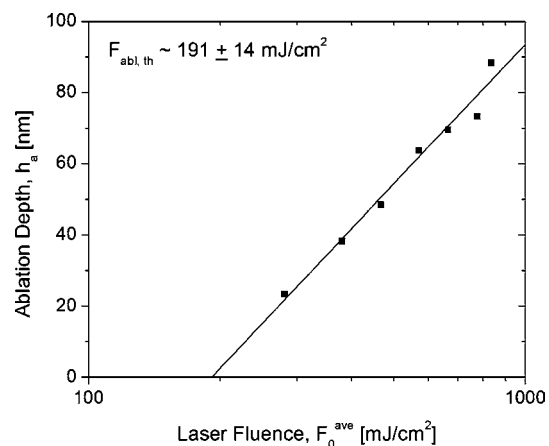


FIGURE 4 The depth of the laser ablated silicon crater is plotted as a function of the laser fluence. Extrapolation of the linear fit to zero provides the single-shot femtosecond laser ablation threshold of silicon

fluences. By extrapolating the linear fit to zero, we find the single-shot ablation threshold of silicon to be $F_{\text{abl,th}} = 191 \pm 14 \text{ mJ/cm}^2$. Uncertainty in the ablation threshold measurement arises mainly due to the error in the measured spot size and pulse-to-pulse energy variability.

Ablation craters generated at laser fluences lower than about 1 J/cm^2 are mediated by the optical penetration depth [26]. In Fig. 4, we only present results within this regime. At 780 nm wavelength, the dominant mechanism of electron excitation is single photon absorption due to the photon energy (1.6 eV) having greater energy than the silicon bandgap (1.14 eV) [27]. Since absorption is linear, the ablation profile will resemble the intensity distribution of the incident light. As the laser fluence is increased above 1 J/cm^2 , thermal effects begin to affect the surrounding lattice. Carrier conduction contributions become important and the electron-driven heat penetration depth defines the ablation depth.

Before the onset of true ablation, i.e., removal of material, irradiation of silicon with a low fluence laser pulse can result in surface modification. Below the ablation threshold, the molten layer will resolidify either into an amorphous or

re-crystallized state. The amorphous region marks the lowest input energy needed to achieve modification. The molten layer resolidifies faster than the re-crystallization time scale, leaving it in an amorphous state [28]. The single shot modification threshold for silicon(100) was estimated to be about 186 mJ/cm^2 . This threshold was determined from the data presented in Fig. 2, where the linear fit was extrapolated to zero.

3.2 Effect of gold nanoparticles on silicon ablation

Figure 5a shows an SEM image of a nanoparticle studded silicon(100) wafer after irradiation by an elliptically shaped laser pulse of 190 mJ/cm^2 average fluence. In Fig. 5b, a Gaussian curve representing the peak incident fluence along the short axis is given as a reference to the different ablation regimes along the irradiation zone. The spatial profile of a Gaussian beam is given by

$$F(r) = F_0^{\text{peak}} \exp\left(-\frac{2r^2}{w_0^2}\right), \quad (5)$$

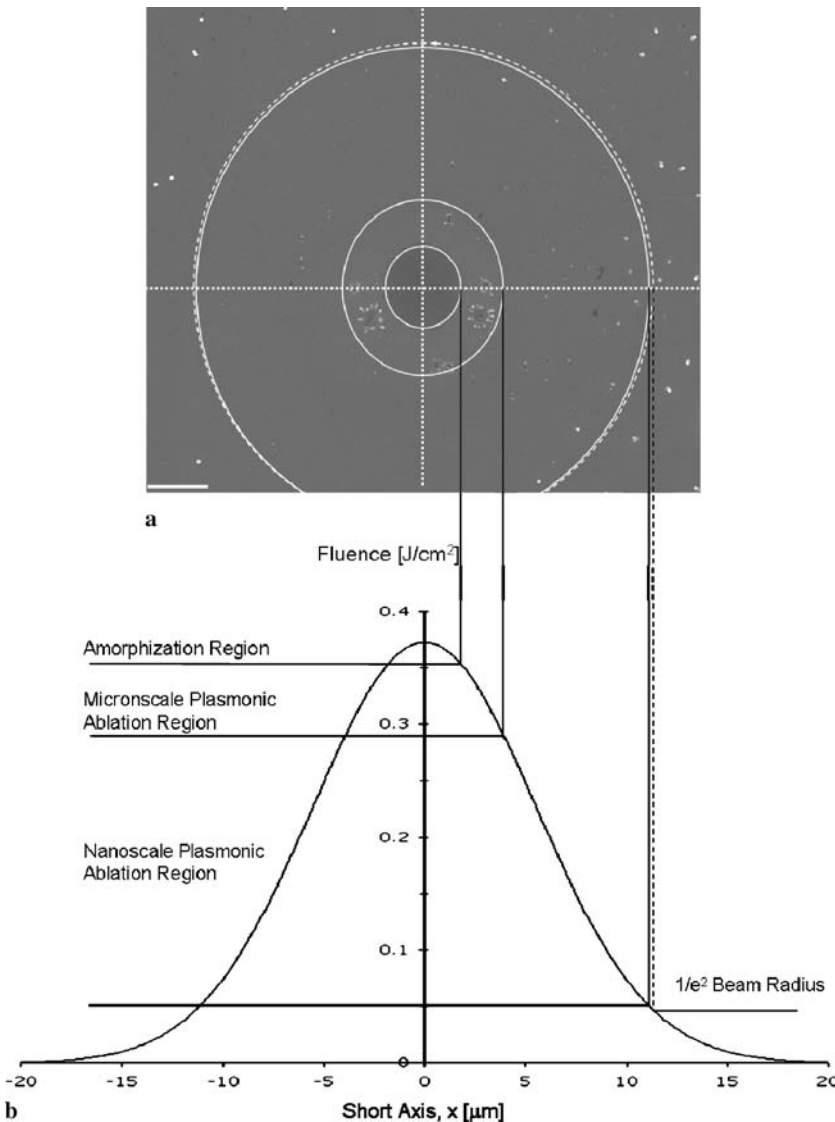


FIGURE 5 An SEM image of nanoparticles deposited on silicon substrate after laser irradiation (a) and the corresponding Gaussian distribution of the laser beam (b). A 190 mJ/cm^2 average fluence is directed orthogonally to the substrate (normal incidence). Several regions of ablation can be ascertained from the image. The scale bar is $3 \mu\text{m}$

where F_0^{peak} is the laser peak fluence and r is the distance from the center of the beam. Typically the fluence is given in terms of an average value instead of the peak fluence, as is such in this text. The average fluence can be determined by

$$F_0^{\text{ave}} = \frac{E_{\text{pulse}}}{\pi w_0^2}. \quad (6)$$

The incident pulse was directed such that it was orthogonal to the substrate surface with the \mathbf{E} -field along the short axis of the elliptical pulse. The application of a laser pulse having a Gaussian intensity distribution allows for a broad range of laser fluences to be studied in a single experiment. Several identifiable regions of surface modification are observable. In increasing distance from irradiation center these regions are:

1. Amorphization of Si(100): In the center, there is a region of surface modification due to the amorphization of Si(100). In this region, no material is removed from the substrate, which is confirmed with AFM. The surface roughness, however, increases to about 5 nm. Amorphization occurs until the laser fluence drops to approximately 176 mJ/cm², which agrees with the modification threshold stated earlier in the paper. All particles in this region are completely ablated and any plasmonic effect is washed out due to long silicon melt times.
2. Ablation induced by local enhancement near the particles: Here we observe a region of surface ablation on the micronscale induced by the laser enhancement in the near-field of the particles. The ablation craters are surrounded by a region of surface melt. Generally, rim structures and splash zones border the melt zones. Again, particles are completely ablated at this laser fluence level.
3. Ablation at the nanoscale via local enhancement near the particles: The enhancement in the vicinity of the particles generates nanoscale craters on the silicon surface that are direct imprints of the dipolar scattering pattern with any surrounding damage to the silicon lattice. Here, the laser fluence is not large enough to completely ablate the particle. The collective oscillations of electrons (surface plasmons) in the nanoparticle cause the particle to split into two halves as will be shown later in the paper. The molten gold generally resolidifies at the outer edges of the ablation crater. In the case of plasmonic ablation for nanolithography applications, it would be ideal to work in this fluence level. Material removal only extends tens of nanometers from the particle center and is confined to the nanoscale.
4. No surface modification/ablation: The incident laser fluence continues to decrease such that the local enhancement generated by the particle is not enough to overcome the modification threshold of the silicon substrate. As described later in the paper, this ablation limit occurs at an average fluence of 27.5 mJ/cm², when the laser polarization is oriented parallel to the silicon surface. Beyond this point, both silicon and gold remain intact.

3.3 Ablation threshold for gold nanospheres

We determined the gold nanoparticle ablation threshold between 20 to 25 mJ/cm², which we define as the

laser fluence below which the whole spherical structure of the particle remains intact. This value is in good agreement with the recently reported damage threshold value of 15.5 mJ/cm² for nanospheres of 38 nm in diameter irradiated by 400 nm, 100 fs laser pulses [29]. In those studies, picosecond X-ray scattering measurements revealed that partial material removal from the poles of the nanoparticle occurs for fluences above 15.5 mJ/cm². Below 20–25 mJ/cm², we may expect some material removal to occur, reducing the overall size of the particle in regions of intense scattering. In cases where the plasmonic ablation threshold of silicon is lower than the ablation threshold of the gold particle, nanocrater structures may form underneath the particle itself for fluences down to the threshold value.

3.4 Effects of laser polarization on nanocrater morphology

We studied the effect of laser polarization on the morphology of ablated nanostructures. Figure 6 presents AFM images and cross-sectional profiles of three nanocraters obtained using different cases of laser polarizations. In each case, the scattering pattern in the particle near-field was directly imprinted into the silicon surface. When the incident radiation \mathbf{E} -field is directed at a 45° angle into the silicon substrate surface (p -polarized laser light), only one lobe of the dipolar scattering region interacts with the underlying substrate, leading to the formation of a single circular crater. In Fig. 6a, the relative fluence interacting with the particle was 88 mJ/cm². A crater having a 100 nm diameter and 53 nm maximum depth was generated. Images of craters produced by laser polarizations parallel to the substrate surface when the substrate is angled 0° and 45° to the incident irradiation (s -polarized laser light) are shown in Fig. 6b–c, respectively. In each of the cases, when the laser polarization is parallel to the substrate surface, the generated craters have a double lobed crater structure, which follows the dipolar scattering pattern of the nanoparticle. We find resolidified gold at the ends of each dipolar crater structure after ablation. In Fig. 6, the gold can be clearly visualized and is represented as the peak(s) surrounding the craters in the cross-sectional profiles.

3.5 Plasmonic laser nanoablation threshold

For each polarization orientation, we measured the minimum threshold fluence for plasmonic nanoablation. The maximum depth of generated nanocraters for a broad range of laser fluences is measured using AFM and plotted against the average fluence that interacted with the particle at that point. Determination of the relative fluence at the point of particle ablation is nontrivial in those cases where sample irradiation was at an angle. Each nanocrater rests on a distinct plane some distance above the beam waist, which can be determined according to its location on the substrate. Since the sample is located at a distance above the Rayleigh range, the spot size interacting at the sample plane will change according to height. Each distinct plane will have a unique spot size that can be found using (2). Determination of the relative fluence at the nanocrater location results from projecting each nanocrater onto its corresponding ablation plane. As shown

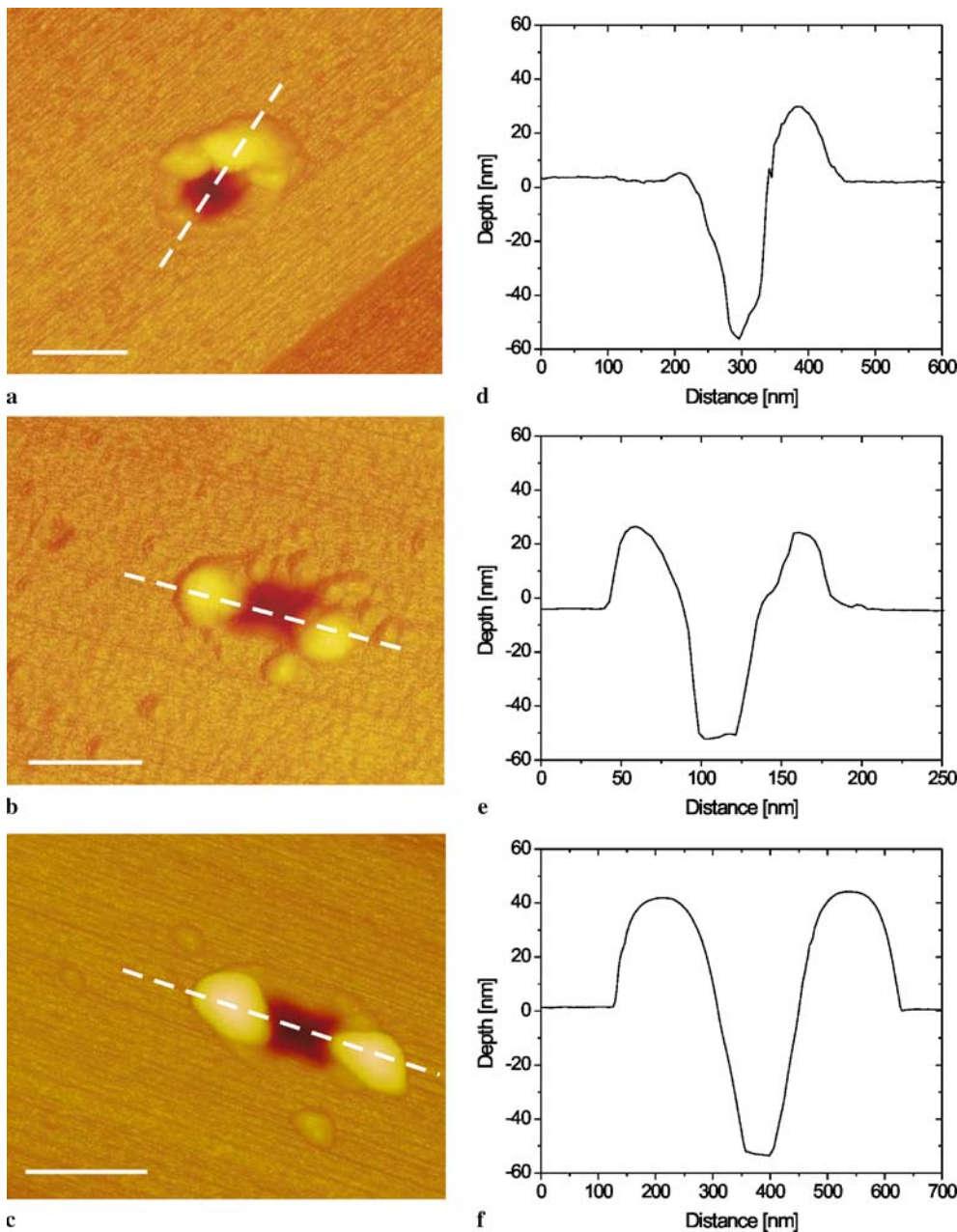


FIGURE 6 AFM images of nano-craters ablated by 150 nm gold nanoparticles on silicon (100) and corresponding cross sections as found along the white dotted line: (a) and (d) 88 mJ/cm² pulse fluence having *p*-polarization at 45° incident angle, (b) and (e) 58 mJ/cm² pulse fluence having normal incidence, and (c) and (f) 128 mJ/cm² pulse fluence having *s*-polarization at 45° incident angle. The scale bars are 200 nm

in Fig. 7, a linear fit to data points follows the relationship given in (4). Extrapolation of the linear fit line to zero provides the “enhanced single-shot ablation threshold”. For *p*-polarized laser light at 45°, the required fluence for surface ablation is reduced to 8.2 ± 2.9 mJ/cm². Ablation thresholds determined for laser polarizations parallel to the substrate surface when the substrate is angled 0° and 45° (*s*-polarized laser light) to the incident irradiation are 27.5 ± 4.3 mJ/cm² and 46.7 ± 16.3 mJ/cm², respectively. The errors were estimated based on the covariance of the data with respect to the linear fit. In (4), both α_{eff}^{-1} and $\alpha_{\text{eff}}^{-1} \ln(F_{\text{th,abl}})$ have an associated error. From these errors, we can calculate a set of linear fits that will provide a range of possible ablation thresholds.

The near-field enhancement factor is a measure of the particles ability to efficiently collect light from a cross-

section larger than its geometrical cross-section and scatter it into a nanoscale region necessary for material ablation. Nedyalkov et al. previously determined the near-field enhancement factor by finding the ratio of the lasers fluences required to achieve the same ablation depth with and without nanoparticles present on the substrate [13]. In the current paper, we propose the use of the “standard single-shot ablation threshold” as found from h_a measurements in estimating the nanoparticle near-field enhancement factor. The experimental near-field enhancement factor is estimated using the relationship $\gamma_{\text{eff}} = F_{\text{th}}/F_{\text{th}}^{n_p}$. For the *p*-polarized irradiation of a particle at a 45° angle, the relationship gives an experimental near-field enhancement of $\gamma_{\text{eff}} = 23.1 \pm 7.6$. Normal incidence and *s*-polarized light at 45° give enhancements of $\gamma_{\text{eff}} = 6.9 \pm 0.6$ and $\gamma_{\text{eff}} = 4.1 \pm 1.3$, respectively.

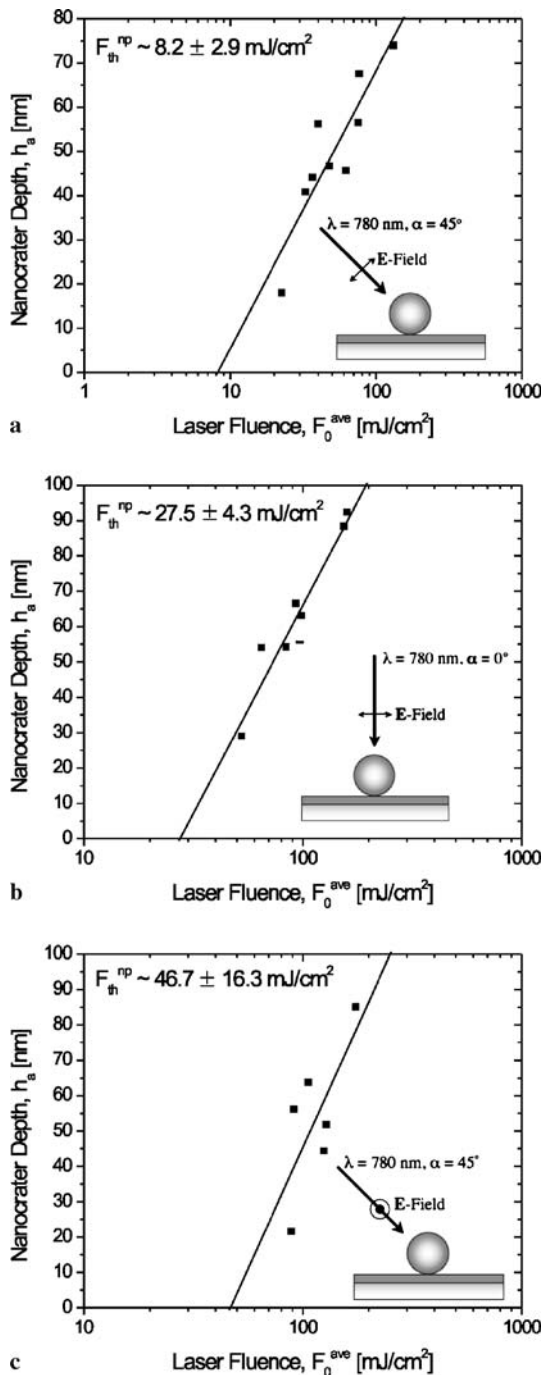


FIGURE 7 Crater depths generated by single 150 nm gold particles are measured at various laser fluences. The depths of the ablation craters are plotted as a function of the laser fluence. Extrapolation of the linear fit to zero provides the enhanced sing-shot ablation threshold. Plots for three different polarizations types were generated: (a) *p*-polarization at 45° incident angle, (b) normal incidence, and (c) *s*-polarization at 45° incident angle

3.6 Comparison to theoretical calculations

To validate our measurements, we calculated the near-field intensity based on the solution of the boundary-value problem for a spherical particle on a flat semi-infinite substrate [30]. It is assumed that an incident plane wave with a wavelength of 780 nm propagates along the *z*-coordinate. The angle of irradiation and direction of the electric field are varied

according to polarization type. The particle is 150 nm in diameter. Additional multi-reflections between the particle and the substrate, which can lead to further intensity variation along the surface, are taken into account. For a transparent particle on the substrate irradiated with normal incidence, the intensity absorbed by the substrate can be estimated by the following relationship [31]:

$$I \approx \frac{I_0 (1 - R)}{1 - b R}, \quad (7)$$

where I_0 is the Mie intensity around the particle when it is not resting on a substrate, R is the substrate reflectivity, and b is the back-scattering efficiency of the particle. When $b < 1$, the intensity will be smaller and for $b > 1$, the intensity will be higher than the Mie intensity. The native oxide layer was ignored because of its negligible effect on the substrate refractive indices.

Two sets of calculations were performed to determine the effect of the incident pulse energy absorption by the silicon.

1. Initial experiments are completed with the silicon at room temperature, having optical constants $n = 3.930$ and $\kappa = 0.136$. In this case, the silicon surface does not interact with the incident pulse and the field enhancement around the particle was due solely to the interaction of the laser pulse with the particle. The optical constants of the 150 nm gold particle are calculated using the Drude free electron model, giving $n = 0.195$ and $\kappa = 4.910$ [20].
2. In the second case, we assumed the formation of a low-density plasma along the silicon surface. Here the silicon interacts with the incident pulse by absorbing some of the incident pulse energy. It was assumed that a steady-state plasma was formed at the exact onset of the pulse. Experimentally this will not be the case, for free electrons will be generated continually over the pulse duration, increasing the surface absorptivity and reflectivity with time. For this general case, optical constants for silicon were given as $n = 4.0$ and $\kappa = 4.5$ [32].

Figure 8 shows the calculated field intensity, i.e., the Poynting vector, along the substrate surface for both cases. First, we shall look at the theoretical enhancement for irradiation with *p*-polarized light angled at 45°. We find an enhancement of 17.2 for the first case and 23.9 for the second. This shows that the absorption of the incident energy by the silicon has a large effect on the near-field enhancement of the particle. For simplicity in the calculation, we assumed the formation of a steady-state plasma, but in reality, a plasma with time-dependent density will form during the pulse duration. This agrees with the found experimental results, where the measured field enhancement is between the two theoretical values. As the silicon absorbs the incident energy over the pulse duration, the absorptivity and reflectivity of the silicon will continue to increase, generating larger enhancements in the particle vicinity.

For normal incidence and the *s*-polarization cases, we find larger experimental values than that presented theoretically. A number of factors could be contributing to the increased enhancement. We believe a large part of the extra enhancement contributed to the experimental results for normal incidence is due to increased surface reflectivity, causing a larger num-

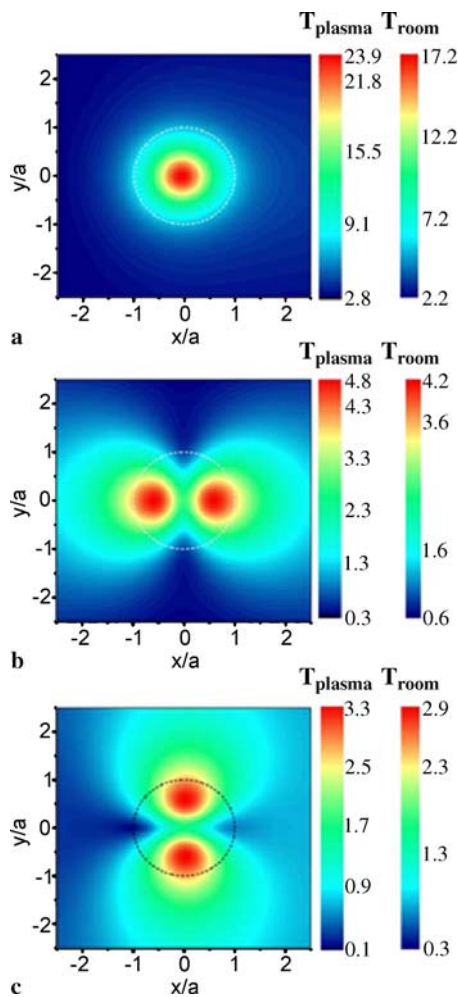


FIGURE 8 Calculated field intensity along the substrate surface, which is based on the solution of the boundary-value problem for a spherical particle on a flat semi-infinite substrate. The 150 nm particle is labeled as the *dotted circle*. T_{plasma} and T_{room} describe the field enhancement with and without the addition of the low density plasma generated along the silicon surface, respectively. (a) p -polarization at 45° incident angle, (b) normal incidence, and (c) s -polarization at 45° incident angle

ber of reflections from the silicon surface to interact with the particle. The reflected waves off the surface will directly interact with the particle. In the s -polarized at 45° irradiation case, most of the wave is reflected at an angle away from the particle. Only a small part of the reflected wave interacts with the particle. We see a slight increase in enhancement beyond the theoretically calculated value. Additional factors could include other nonlinear effects due to the ultrashort laser pulses or ultrasmall confinement of light or phase changes in the gold particle during irradiation.

4 Conclusion

We demonstrated the nanoscale ablation of silicon(100) using the plasmonic enhancement of femtosecond laser pulses in the near-field of spherical gold particles. The influence of laser polarization and angle of ablation on generated craters were investigated and characterized by AFM and SEM. It was found that there is a linear relationship between crater depth and the logarithm of the average laser fluence.

Extrapolation of the linear relationship to zero provides the enhanced single-shot ablation threshold. Results show that particles irradiated with p -polarized light have the greatest enhancement, reducing the required fluence for silicon ablation by 23.1 ± 7.6 times. Normal incident light reduced the ablation threshold by 6.9 ± 0.6 times, while s -polarized light at 45° had a 4.1 ± 1.3 times reduction. Measured crater morphologies, as predicted in our theoretical calculations, were direct imprints of the dipolar scattering region around the particle. The measured near-field enhancement values agree well with the maximum field enhancements obtained in our calculations. Agreement between theory and measurements supports that the nanocraters were indeed formed by the enhanced plasmonic scattering in the near-field of the nanoparticles. The formation of a low-density plasma on the surface due to the incident laser pulse was found to increase the particle enhancement at the substrate surface.

The results presented here are only the first steps toward near-field optical processing of materials. With further advances in nanoparticle deposition techniques, this type of ablative technology has the potential to directly impact the fields of laser-assisted nanomachining and nanolithography, providing a patterning method not limited by diffraction and achieving high throughput with reduced production costs. Additionally, the use of antibody specific gold bioconjugates presents the possibility for plasmonic laser nanosurgery, which could be used to manipulate molecules and subcellular structures. In future papers, we will explore the ablation of dielectric substrates and the macro-ablation of cellular materials to determine the appropriate fluence necessary for cellular processing.

ACKNOWLEDGEMENTS We thank William Lackowski for his assistance with the AFM, Frederic Bourgeois and Chris Hoy for their help with spot size measurements, and Amber Doiron and Tania Betancourt for their help with the SEM. We acknowledge funding of this research by the National Science Foundation grant BES-0508266 and State of Texas Advanced Research Initiative and partial funding of the AFM and SEM facilities by The Robert A. Welch Foundation.

REFERENCES

- 1 A.A. Gorbunov, W. Pompe, Phys. Stat. Solidi A **145**, 333 (1994)
- 2 J. Jearsch, F. Demming, L.J. Hildenhausen, K. Dickmann, Appl. Phys. A **66**, 29 (1997)
- 3 K. Wilder, C.F. Quate, D. Adderton, R. Bernstein, V. Elings, Appl. Phys. Lett. **77**, 2527 (1998)
- 4 A. Chimmalgi, C.P. Grigoropoulos, K. Komvopoulos, J. Appl. Phys. **97**, 104319 (2005)
- 5 S. Nolte, B.N. Chichkov, H. Welling, Y. Shani, K. Lieberman, H. Terkel, Opt. Lett. **24**, 914 (1999)
- 6 L. Wang, E.X. Jin, S.M. Uppuluri, X. Xu, Opt. Express **14**, 9902 (2006)
- 7 D.J. Hwang, A. Chimmalgi, C.P. Grigoropoulos, J. Appl. Phys. **99**, 044905 (2006)
- 8 W. Srituravanich, N. Fang, C. Sun, Q. Luo, X. Zhang, Nano Lett. **4**, 1085 (2004)
- 9 S.M. Huang, M.H. Hong, B. Luk'yanchuk, T.C. Chong, Appl. Phys. A **77**, 293 (2003)
- 10 W. Cai, R. Piestun, Appl. Phys. Lett. **88**, 111112 (2006)
- 11 A.J. Heltzel, A. Battula, J.R. Howell, S.C. Chen, J. Heat Transf. **129**, 53 (2007)
- 12 S.M. Huang, M.H. Hong, B. Luk'yanchuk, T.C. Chong, Appl. Phys. Lett. **82**, 4809 (2003)
- 13 N.N. Nedyalkov, H. Takada, M. Obara, Appl. Phys. A **85**, 163 (2006)
- 14 N.N. Nedyalkov, T. Sakai, T. Miyaniishi, M. Obara, J. Phys. D Appl. Phys. **39**, 5037 (2006)

- 15 P. Leiderer, C. Bartels, J. König-Birk, M. Mosbacher, J. Boneberg, *Appl. Phys. Lett.* **85**, 5370 (2004)
- 16 M.F. Yanik, H. Cinar, H.N. Cinar, A.D. Chisholm, Y. Jin, A. Ben-Yakar, *Nature* **432**, 822 (2004)
- 17 U.K. Tirlapur, K. König, *Nature* **418**, 290 (2002)
- 18 N. Shen, D. Datta, C.B. Schaffer, P. LeDuc, D.E. Ingber, E. Mazur, *Mech. Chem. Biosyst.* **2**, 17 (2005)
- 19 A. Vogel, J. Noack, G. Huttman, G. Paltauf, *Appl. Phys. B* **81**, 1015 (2005)
- 20 H. Hovel, S. Fritz, A. Hilger, U. Kreibig, M. Vollmer, *Phys. Rev. B* **48**, 178 (1993)
- 21 S. Nolte, B.N. Chichkov, H. Welling, Y. Shani, K. Lieberman, H. Terkel, *Opt. Lett.* **24**, 914 (1999)
- 22 J.M. Liu, *Opt. Lett.* **7**, 196 (1982)
- 23 A. Ben-Yakar, R.L. Byer, *J. Appl. Phys.* **98**, 5316 (2004)
- 24 B.J. Messinger, K. Ulrich von Raben, R.K. Chang, P.W. Barber, *Phys. Rev. B* **24**, 649 (1981)
- 25 M. Quinten, *Appl. Phys. B* **73**, 245 (2001)
- 26 S. Nolte, C. Momma, H. Jacobs, A. Tunnermann, B.N. Chichkov, B. Wellegehausen, H. Welling, *J. Opt. Soc. Am. B* **14**, 2716 (1997)
- 27 S.K. Sundaram, E. Mazur, *Nature Mater.* **1**, 217 (2002)
- 28 J. Bonse, S. Baudach, J. Kruger, W. Kautek, M. Lenzer, *Appl. Phys. A* **74**, 19 (2002)
- 29 A. Plech, V. Kotaidis, M. Lorenc, J. Boneberg, *Nature Phys.* **2**, 44 (2006)
- 30 B.S. Luk'yanchuk, Z.B. Wang, W.D. Song, M.H. Hong, *Appl. Phys. A* **79**, 747 (2004)
- 31 Y.W. Zheng, Dissertation, National University of Singapore (2002), pp. 57–59
- 32 G.R. Jellison Jr., D.H. Lowndes, *Appl. Phys. Lett.* **51**, 352 (1987)